J. Fluid Mech. (2017), *vol.* 814, *pp.* 249–276. © Cambridge University Press 2017
doi:10.1017/jfm.2016.795

Small perturbation evolution in compressible Poiseuille flow: pressure–velocity interactions and obliqueness effects

Zhimin Xie[1], **Mona Karimi**[1,2,†] **and Sharath S. Girimaji**[1,3]

[1]Aerospace Engineering Department, Texas A&M University, College Station, TX 77843, USA

[2]Department of Mathematics, Texas A&M University, College Station, TX 77843, USA

[3]Ocean Engineering Department, Texas A&M University, College Station, TX 77843, USA

(Received 7 June 2016; revised 10 November 2016; accepted 14 November 2016;
first published online 3 February 2017)

Small perturbation evolution in compressible Poiseuille flow is contrasted against the incompressible case using direct simulations and non-modal linear analysis. The onset of compressibility effects leads to a profound change in the behaviour of pressure and its interaction with the velocity field. Linear analysis shows that the most significant compressibility outcome is the harmonic coupling between pressure and wall-normal velocity perturbations. Oscillations in normal perturbations can lead to periods of negative production causing suppression of perturbation growth. The extent of the influence of compressibility can be characterized in terms of an effective gradient Mach number (M_g^e). Analysis shows that M_g^e diminishes as the angle of the perturbation increases with respect to the shear plane. Direct numerical simulations show that streamwise perturbations, which would lead to Tollmien–Schlichting instability in the incompressible case, are completely suppressed in the compressible case and experience the highest M_g^e. At the other extreme, computations reveal that spanwise perturbations, which experience negligible M_g^e, are entirely unaltered from the incompressible case. Perturbation behaviour at intermediate obliqueness angles is established. Moreover, the underlying pressure–velocity interactions are explicated.

Key words: compressible boundary layers, compressible flows

1. Introduction

Poiseuille flow has long served as the archetypal flow for examining near-wall instability, transition and turbulence phenomena (Landahl 1980; Thomson 1887; Butler & Farrell 1992; Schmid & Henningson 2001). This flow embodies much of the fundamental physical features of complex engineering boundary layers without many of the undue complications. Poiseuille flow is ideally suited for examining the fundamental effects of compressibility on wall-bounded shear flows at high Mach numbers. With increasing Mach number, pressure undergoes a profound change in character. At low Mach numbers, hydrodynamic pressure is a Lagrange multiplier (Reddy 1984) with the only function of preserving the divergence-free velocity field.

---

† Email address for correspondence: monak16mpi@gmail.com

The resulting low Mach number velocity field is solenoidal in character. At higher Mach numbers, pressure is a *bona fide* thermodynamic state variable and its evolution is governed by energy and state equations. Pressure then exhibits wave behaviour, leading to the emergence of a dilatational (wave-like) component of the velocity field. This leads to profound changes in pressure–velocity interactions which affects flow stability and turbulence. The objective of the present work is to contrast the evolution of small perturbations in Poiseuille flow at high and low Mach numbers. The focus is on understanding the influence of changing pressure–velocity interaction on perturbation evolution at different speeds. The interactions are first examined by performing linear analysis of compressible Poiseuille flow and then the inferences are verified against temporal direct numerical simulations (DNS).

In the literature, linear stability theory employing eigenvalue analysis is generally used to examine modal perturbation growth in fluid flows. Since the focus of this work is on understanding the transient pressure–velocity interaction mechanism and its influence on perturbation growth, we perform non-modal initial value analysis of the linearized governing equations along the lines of rapid distortion theory (RDT) – see Simone, Coleman & Cambon (1997) and Livescu & Madnia (2004).

In recent years, the present group has been developing insight into the pressure–velocity interactions and perturbation growth in homogeneous shear flows (Bertsch, Suman & Girimaji 2012; Lavin *et al.* 2012; Kumar, Bertsch & Girimaji 2014; Kumar *et al.* 2015; Lee, Venugopal & Girimaji 2016). Findings from these studies of homogeneous shear turbulence are invaluable for understanding Poiseuille flow behaviour. The major results from previous studies are now summarized.

(i) Using RDT, Lavin *et al.* (2012) establishes that the evolution of turbulent kinetic energy of an isotropically distributed ensemble of perturbation wave vectors in high Mach number homogeneous shear flow exhibits a three-stage evolution. The three stages are demarcated on the basis of the relative magnitude of shear and acoustic time scales. Thus, the shear–acoustic time scale ratio is established as an important parameter influencing perturbation growth.

(ii) In Bertsch *et al.* (2012), the energy exchange between potential energy (pressure) and dilatational kinetic energy is investigated using RDT. Energy redistribution between different Reynolds stress components is also established.

(iii) The influence of wave vector orientation on perturbation growth in compressible homogeneous shear flow is examined using RDT and DNS in Kumar *et al.* (2014).

(iv) Potential control strategies for inhibiting turbulent kinetic energy growth in shear homogeneous flows at high Mach numbers are examined in Kumar *et al.* (2015).

(v) The competition between return-to-isotropy and potential–kinetic energy equipartition in anisotropic decaying dilatational turbulence is investigated in Lee *et al.* (2016) using DNS.

The above studies establish the nature of interactions between pressure and velocity fields in homogeneous turbulence. In Karimi & Girimaji (2016), linear analysis and DNS are extended to mixing layers. It is shown that the wave-like dilatational velocity field disrupts the Kelvin–Helmholtz rollers inhibiting roll up, instability and thus mixing in high-speed flows. The pressure-released limit of Poiseuille flow is examined in (Xie & Girimaji 2014).

The present work examines the effect of compressibility on perturbation growth in compressible Poiseuille flow. One of the key objectives of this work is to investigate the effect of the dilatational field on Tollmien–Schlichting waves which initiate transition to turbulence in many boundary layers of practical importance. The focus of the work is to understand compressibility-induced physical mechanisms that influence perturbation evolution. The principal goal is to explain the transient behaviour in the context of changing pressure–velocity interactions with increasing Mach number. While this insight is important for developing transition and turbulence models, such efforts are deferred to future works. We perform the following studies.

(i) Analyse the initial value problem arising from the linearized perturbation equations to compare and contrast the pressure–velocity interactions in incompressible and compressible flows. The role of perturbation mode orientation with respect to the shear plane is examined.
(ii) Perform temporally evolving direct numerical simulations of small perturbation growth in compressible Poiseuille flow with a parabolic base field sustained by suitable forcing. The base temperature and pressure fields are determined from the requirement that the parabolic velocity field is a steady state solution of the governing equations. Both adiabatic and isothermal wall boundary conditions are considered. The simulations cover a wide range of Mach and Reynolds numbers.
(iii) Use linear analysis and DNS results to develop a clear physical explanation of the pressure–velocity interactions and their effect on the transient evolution of small perturbations in wall-bounded high-speed flows.

The governing equations and linear analysis are presented in § 2. A brief introduction of the numerical approach is given in § 3. The DNS results are presented in § 4. The results and the outcome of linear analysis are used to develop a physical explanation of the underlying pressure–velocity interactions. We close in § 5 with a summary of the salient contributions.

2. Governing equations and linear analysis

The compressible Navier–Stokes equations along with ideal-gas law form the basis of this study:

$$\frac{\partial \rho}{\partial t} + \frac{\partial}{\partial x_j}(\rho u_j) = 0, \tag{2.1}$$

$$\frac{\partial u_i}{\partial t} + u_j \frac{\partial u_i}{\partial x_j} = \frac{1}{\rho}\frac{\partial \tau_{ij}}{\partial x_j}, \tag{2.2}$$

$$\rho c_v \left(\frac{\partial T}{\partial t} + u_j \frac{\partial T}{\partial x_j}\right) = \frac{\partial}{\partial x_j}\left(k \frac{\partial T}{\partial x_j}\right) + \tau_{ij} e_{ij}, \tag{2.3}$$

$$p = \rho R T, \tag{2.4}$$

where ρ is the fluid density, u_i is velocity component, T is temperature, p is the gas pressure, τ_{ij} is the full stress tensor, e_{ij} is the rate of strain tensor, c_v is the specific heat at constant volume, k is the coefficient of thermal conductivity, R is the specific gas constant, x_i is the spatial coordinate and t is time. The rate of strain and stress tensors are given by:

$$e_{ij} = \frac{1}{2}\left(\frac{\partial u_i}{\partial x_j} + \frac{\partial u_j}{\partial x_i}\right), \tag{2.5}$$

$$\tau_{ij} = 2\mu\ e_{ij} + \left[\tfrac{2}{3}(\lambda - \mu) e_{kk} - p\right] \delta_{ij}, \tag{2.6}$$

where μ is the coefficient of dynamic viscosity, λ is the coefficient of second viscosity and δ_{ij} is the Kronecker delta. We consider a calorically perfect gas and set the Prandtl number (Pr) to 0.7. The specific heat ratio γ is 1.4. The dynamic viscosity is assumed to follow Sutherland's law (Heiser & Pratt 1994):

$$\mu = \mu_0 \left(\frac{T}{T_0}\right)^{2/3} \frac{T_0 + C}{T + C}, \tag{2.7}$$

where T_0 is the reference temperature which is 273.15 K, μ_0 is the viscosity at reference temperature which is 1.716×10^{-5} kg m s^{-1} and C is the Sutherland temperature which is 110.4 K. The DNS performed in this study solve the full set of equations. The analysis is however restricted to linearized equations.

2.1. *Linear analysis*

The objective of the study is to examine small perturbation evolution in a compressible parallel shear flow subject to the above conservation and state equations. The flow and thermodynamic variables are decomposed into base and perturbation fields:

$$\rho = \bar{\rho} + \rho'; \quad u_i = \bar{U}_i + u_i'; \quad p = \bar{p} + p'; \quad T = \bar{T} + T', \tag{2.8a–d}$$

where $\bar{(\cdot)}$ and $(\cdot)'$ represent the base/background flow and the perturbation field, respectively. The base flow satisfies the following equations:

$$\frac{\partial \bar{\rho}}{\partial t} + \frac{\partial \bar{\rho} \bar{U}_i}{\partial x_i} = 0, \tag{2.9}$$

$$\frac{\partial \bar{U}_i}{\partial t} + \bar{U}_j \frac{\partial \bar{U}_i}{\partial x_j} = -\frac{1}{\bar{\rho}} \frac{\partial \bar{p}}{\partial x_i} + \frac{1}{\bar{\rho}} \frac{\partial}{\partial x_j} \left[\mu \left(\frac{\partial \bar{U}_i}{\partial x_j} + \frac{\partial \bar{U}_j}{\partial x_i}\right)\right] + \frac{1}{\bar{\rho}} \frac{\partial}{\partial x_i} \left[\frac{2}{3}(\lambda - \mu) \frac{\partial \bar{U}_j}{\partial x_j}\right], \tag{2.10}$$

$$\frac{\partial \bar{p}}{\partial t} + \bar{U}_j \frac{\partial \bar{p}}{\partial x_j} = -\bar{p}\gamma \frac{\partial \bar{U}_k}{\partial x_k} + \bar{f}(k) + \bar{g}(\mu), \tag{2.11}$$

where $\bar{f}(k)$ and $\bar{g}(\mu)$ denote the effects of heat conduction and viscous transport on the base field, defined as:

$$\bar{f}(k) = \frac{R}{c_v} \frac{\partial}{\partial x_j} \left(\overline{k \frac{\partial T}{\partial x_j}}\right), \tag{2.12}$$

$$\bar{g}(\mu) = \frac{R}{c_v} \left[2\overline{\mu\, e_{ij} e_{ij}} + \frac{2}{3}\overline{(\lambda - \mu) e_{kk} e_{kk}}\right]. \tag{2.13}$$

2.1.1. *Simplifying assumptions for Poiseuille flows*

In this work, the base flow is a planar shear flow with parallel streamlines:

$$\bar{U}_i = (\bar{U}_1(x_2), 0, 0) \text{ leading to } \partial \bar{U}_i / \partial x_i = 0. \tag{2.14}$$

Here, x_1 is defined as the streamwise direction, x_2 is the wall-normal direction and x_3 is the spanwise direction. In numerical simulations, this velocity field is sustained using appropriate forcing (Xie & Girimaji 2014). Due to body-force type of forcing, the background density and pressure fields are nearly spatially invariant to linear order. Thus for the purpose of analysis we assume

$$\bar{\rho}(\boldsymbol{x}) \approx \text{Const.}; \quad \bar{p}(\boldsymbol{x}) \approx \text{Const.} \tag{2.15a,b}$$

A perturbation is introduced into the background field and its subsequent evolution is the subject of the numerical simulations and linear analysis. The nonlinear effects and variations in fluid properties such as viscosity and heat conductivity are neglected in the analysis:

$$\mu(\boldsymbol{x}) \approx \text{Const.}; \qquad k(\boldsymbol{x}) \approx \text{Const.} \tag{2.16a,b}$$

In the numerical simulations, however, $\bar{\rho}$, $\bar{p}$, μ and k vary according to the governing equations.

2.1.2. *Perturbation equations for Poiseuille flows*

By subtracting base flow equations from those of instantaneous flow, the linearized perturbation evolution equations are derived:

$$\frac{\partial \rho'}{\partial t} + \bar{U}_1 \frac{\partial \rho'}{\partial x_1} = -\frac{\partial \bar{\rho} u_k'}{\partial x_k}, \tag{2.17}$$

$$\frac{\partial u_1'}{\partial t} + \bar{U}_1 \frac{\partial u_1'}{\partial x_1} = -\frac{1}{\bar{\rho}}\frac{\partial p'}{\partial x_1} - u_2'\frac{\partial \bar{U}_1}{\partial x_2} + \frac{\mu}{\bar{\rho}}\frac{\partial}{\partial x_j}\left(\frac{\partial u_1'}{\partial x_j} + \frac{\partial u_j'}{\partial x_1}\right) + \frac{2(\lambda-\mu)}{3\bar{\rho}}\frac{\partial}{\partial x_1}\left(\frac{\partial u_j'}{\partial x_j}\right), \tag{2.18}$$

$$\frac{\partial u_2'}{\partial t} + \bar{U}_1 \frac{\partial u_2'}{\partial x_1} = -\frac{1}{\bar{\rho}}\frac{\partial p'}{\partial x_2} + \frac{\mu}{\bar{\rho}}\frac{\partial}{\partial x_j}\left(\frac{\partial u_2'}{\partial x_j} + \frac{\partial u_j'}{\partial x_2}\right) + \frac{2(\lambda-\mu)}{3\bar{\rho}}\frac{\partial}{\partial x_2}\left(\frac{\partial u_j'}{\partial x_j}\right), \tag{2.19}$$

$$\frac{\partial u_3'}{\partial t} + \bar{U}_1 \frac{\partial u_3'}{\partial x_1} = -\frac{1}{\bar{\rho}}\frac{\partial p'}{\partial x_3} + \frac{\mu}{\bar{\rho}}\frac{\partial}{\partial x_j}\left(\frac{\partial u_3'}{\partial x_j} + \frac{\partial u_j'}{\partial x_3}\right) + \frac{2(\lambda-\mu)}{3\bar{\rho}}\frac{\partial}{\partial x_3}\left(\frac{\partial u_j'}{\partial x_j}\right), \tag{2.20}$$

$$\frac{\partial p'}{\partial t} + \bar{U}_1 \frac{\partial p'}{\partial x_1} = -\bar{p}\gamma\left(\frac{\partial u_k'}{\partial x_k}\right) + f'(k) + g'(\mu), \tag{2.21}$$

where the functions $f'(k)$ and $g'(\mu)$ represents the linear effects of heat conduction and viscous transport on the perturbation field. For the simplified case considered in this analysis, these function are given by

$$f'(k) = \frac{R}{c_v} k \frac{\partial^2 T'}{\partial x_j^2}, \tag{2.22}$$

$$g'(k) = 2\frac{R}{c_v}\mu \ \overline{e_{ij}} e_{ij}'. \tag{2.23}$$

However, for the more general case that k and μ vary with temperature, the reader is referred to Mack (1984).

The growth in the perturbation kinetic energy is due to the production term: $-u_2'(\partial \bar{U}_1/\partial x_2)$ on the right-hand side of (2.18). It is also important to examine perturbation vorticity evolution. For the sake of comparison between baroclinic and other compressibility effects, we temporarily include the background density variation. From the velocity field, the linearized vorticity perturbation equations can be obtained:

$$\begin{aligned}\frac{\partial \omega_1'}{\partial t} + \bar{U}_1 \frac{\partial \omega_1'}{\partial x_1} = {} & \frac{1}{\bar{\rho}^2}\frac{\partial \bar{\rho}}{\partial x_2}\frac{\partial p'}{\partial x_3} - \frac{\partial \bar{U}_1}{\partial x_2}\frac{\partial u_3'}{\partial x_1} - \frac{\mu}{\bar{\rho}^2}\frac{\partial \bar{\rho}}{\partial x_2}\left(\frac{\partial^2 u_3'}{\partial^2 x_k} - \frac{1}{9}\frac{\partial^2 u_k'}{\partial x_3 \partial x_k}\right) \\ & + \frac{\mu}{\bar{\rho}}\left(\frac{\partial^3 u_3'}{\partial^2 x_k \partial x_2} - \frac{\partial^3 u_2'}{\partial^2 x_k \partial x_3}\right),\end{aligned} \tag{2.24}$$

$$\frac{\partial \omega_2'}{\partial t}+\bar{U}_1\frac{\partial \omega_2'}{\partial x_1} = -\frac{\partial \bar{U}_1}{\partial x_2}\frac{\partial u_2'}{\partial x_3}+\frac{\mu}{\bar{\rho}}\left(\frac{\partial^3 u_1'}{\partial^2 x_k \partial x_3}-\frac{\partial^3 u_3'}{\partial^2 x_k \partial x_1}\right), \tag{2.25}$$

$$\begin{aligned}\frac{\partial \omega_3'}{\partial t}+\bar{U}_1\frac{\partial \omega_3'}{\partial x_1} = {} & \frac{1}{\bar{\rho}^2}\frac{\partial \bar{\rho}}{\partial x_2}\frac{\partial p'}{\partial x_1}-\frac{\partial \bar{U}_1}{\partial x_2}\left(\frac{\partial u_1'}{\partial x_1}+\frac{\partial u_2'}{\partial x_2}\right)-\frac{\mu}{\bar{\rho}^2}\frac{\partial \bar{\rho}}{\partial x_2}\left(\frac{\partial^2 u_1'}{\partial^2 x_k}-\frac{1}{9}\frac{\partial^2 u_k'}{\partial x_1 \partial x_k}\right)\\ & +\frac{\mu}{\bar{\rho}}\left(\frac{\partial^3 u_2'}{\partial^2 x_k \partial x_1}-\frac{\partial^3 u_1'}{\partial^2 x_k \partial x_2}\right)+u_2'\frac{\partial^2 \bar{U}_1}{\partial^2 x_2}.\end{aligned} \tag{2.26}$$

Among the three components, the spanwise vorticity perturbation (ω_3') is the most relevant for shear flow instability investigation as it is central to Tollmien–Schlichting (TS) wave formation. In spanwise vorticity perturbation equation (2.26), multiple mechanisms can be identified. On the right-hand side of (2.26), the first term $(\partial\bar{\rho}/\partial x_2)(\partial p'/\partial x_1)/\bar{\rho}^2$ represents the baroclinic effect, the second term $(\partial \bar{U}_1/\partial x_2)\left(\partial u_1'/\partial x_1+\partial u_2'/\partial x_2\right)$ represents compressible vortex production (CVP), the third and fourth terms denote viscous effects and finally the last term $u_2'(\partial^2\bar{U}_1/\partial^2 x_2)$ is the second derivative effect.

Inspection of the transport equations reveals that instability of shear flows manifest via two critical terms: $u_2'(\partial \bar{U}_1/\partial x_2)$ in the velocity equation (2.19) and $u_2'(\partial^2\bar{U}_1/\partial^2 x_2)$ in the vorticity equation (2.26). Clearly, the evolution of normal perturbation (u_2') plays a major role in determining the instability growth characteristics in both incompressible and compressible shear flows. Thus, the first key challenge is to establish how the change in character of pressure affects the evolution of u_2'. Considering the spanwise vorticity equation, it is evident that the compressibility effects also manifest via the baroclinic and CVP terms. Then, the second challenge is to examine the balance between the second derivative and the compressibility effects.

2.2. *Pressure–velocity interaction in compressible flows*

To examine the pressure–velocity interactions in an arbitrary planar shear flow, we temporarily suppress the viscous terms. The inviscid perturbation equations are:

$$\frac{\partial \rho'}{\partial t}+\bar{U}_1\frac{\partial \rho'}{\partial x_1}=-\frac{\partial \bar{\rho} u_k'}{\partial x_k}, \tag{2.27}$$

$$\frac{\partial u_1'}{\partial t}+\bar{U}_1\frac{\partial u_1'}{\partial x_1}=-\frac{1}{\bar{\rho}}\frac{\partial p'}{\partial x_1}-u_2'\frac{\partial \bar{U}_1}{\partial x_2}, \tag{2.28}$$

$$\frac{\partial u_2'}{\partial t}+\bar{U}_1\frac{\partial u_2'}{\partial x_1}=-\frac{1}{\bar{\rho}}\frac{\partial p'}{\partial x_2}, \tag{2.29}$$

$$\frac{\partial u_3'}{\partial t}+\bar{U}_1\frac{\partial u_3'}{\partial x_1}=-\frac{1}{\bar{\rho}}\frac{\partial p'}{\partial x_3}, \tag{2.30}$$

$$\frac{\partial p'}{\partial t}+\bar{U}_1\frac{\partial p'}{\partial x_1}=-\bar{p}\gamma\left(\frac{\partial u_k'}{\partial x_k}\right). \tag{2.31}$$

To facilitate further analysis, we apply the Howarth–Dorodnitsyn transformation (Howarth 1948). The flow evolution is now described in a coordinate moving with the background convective velocity:

$$X_1=x_1-\int_0^t U_1(x_2)\,\mathrm{d}\xi, \quad X_2=x_2, \quad X_3=x_3, \quad t=t. \tag{2.32a–c}$$

The perturbation equations (2.17)–(2.21) can be rewritten in the new frame as follows:

$$\frac{\mathrm{d}\rho'}{\mathrm{d}t} = -\frac{\partial \bar{\rho} u_1'}{\partial X_1} + \frac{\partial \bar{\rho} u_2'}{\partial X_2} - \frac{\partial \bar{\rho} u_2'}{\partial X_1} \int_0^t \frac{\partial \bar{U}_1}{\partial x_2}\,\mathrm{d}\xi + \frac{\partial \bar{\rho} u_3'}{\partial X_3}, \tag{2.33}$$

$$\frac{\mathrm{d}u_1'}{\mathrm{d}t} = -\frac{1}{\bar{\rho}}\frac{\partial p'}{\partial X_1} - u_2'\frac{\partial \bar{U}_1}{\partial x_2}, \tag{2.34}$$

$$\frac{\mathrm{d}u_2'}{\mathrm{d}t} = -\frac{1}{\bar{\rho}}\frac{\partial p'}{\partial X_2} + \frac{1}{\bar{\rho}}\frac{\partial p'}{\partial X_1}\int_0^t \frac{\partial \bar{U}_1}{\partial x_2}\,\mathrm{d}\xi, \tag{2.35}$$

$$\frac{\mathrm{d}u_3'}{\mathrm{d}t} = -\frac{1}{\bar{\rho}}\frac{\partial p'}{\partial X_3}, \tag{2.36}$$

$$\frac{\mathrm{d}p'}{\mathrm{d}t} = -\bar{p}\gamma\left(\frac{\partial u_1'}{\partial X_1} + \frac{\partial u_2'}{\partial X_2} - \frac{\partial u_2'}{\partial X_1}\int_0^t \frac{\partial \bar{U}_1}{\partial x_2}\,\mathrm{d}\xi + \frac{\partial u_3'}{\partial X_3}\right). \tag{2.37}$$

Without further loss of generality, we will consider perturbation modes that are periodic in X_1 and X_3 with an arbitrary initial profile in the X_2 direction:

$$u_j' = \hat{u}_j(X_2, t)\mathrm{e}^{\mathrm{i}(\kappa_1 X_1 + \kappa_3 X_3)}; \quad p' = \hat{p}\ (X_2, t)\mathrm{e}^{\mathrm{i}(\kappa_1 X_1 + \kappa_3 X_3)}, \tag{2.38a,b}$$

where κ_1 and κ_3 are the initial perturbation wavenumbers in the streamwise and spanwise directions, $\mathrm{i} = \sqrt{-1}$ denotes the unit imaginary number and $(\hat{\cdot})$ denotes the amplitude of the corresponding perturbation mode. The amplitude is a function of time and normal coordinate. By substituting (2.38) into (2.34)–(2.37), evolution equations of the Fourier amplitude of the perturbation field can be obtained:

$$\frac{\mathrm{d}\hat{u}_1}{\mathrm{d}t} = -\mathrm{i}\kappa_1\frac{\hat{p}}{\bar{\rho}} - \hat{u}_2 S, \tag{2.39}$$

$$\frac{\mathrm{d}\hat{u}_2}{\mathrm{d}t} = -\frac{1}{\bar{\rho}}\frac{\partial \hat{p}}{\partial X_2} + \mathrm{i}\kappa_1\frac{\hat{p}}{\bar{\rho}}\int_0^t S\,\mathrm{d}\xi, \tag{2.40}$$

$$\frac{\mathrm{d}\hat{u}_3}{\mathrm{d}t} = -\mathrm{i}\kappa_3\frac{\hat{p}}{\bar{\rho}}, \tag{2.41}$$

$$\frac{\mathrm{d}\hat{p}}{\mathrm{d}t} = -\gamma\bar{p}\left[\mathrm{i}\kappa_1\hat{u}_1 + \frac{\partial \hat{u}_2}{\partial X_2} - \mathrm{i}\kappa_1\hat{u}_2\int_0^t S\,\mathrm{d}\xi + \mathrm{i}\kappa_3\hat{u}_3\right], \tag{2.42}$$

where the background shear in the normal direction, $S(x_2)$ or S, is given by

$$S = \frac{\partial U_1}{\partial X_2}. \tag{2.43}$$

Equations (2.39)–(2.42) constitute the initial value problem of interest. It is established in previous works on homogeneous shear flows (Livescu & Madnia 2004; Kumar *et al.* 2014) that dilatational velocity is generated on the shear plane. Dilatational velocity represents a large fraction of the normal perturbation (u_2') and a small portion of the streamwise component (u_1'). Many of the compressibility effects can be understood by examining the pressure–velocity (p'–u_2') interactions at different speed regimes.

To non-dimensionalize the perturbation equations (2.39)–(2.42), we introduce dimensionless time and space coordinates:

$$t^* = St; \quad x_i^* = \kappa x_i, \tag{2.44a,b}$$

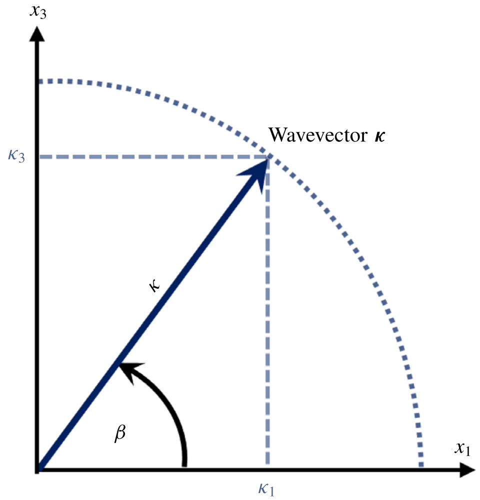

FIGURE 1. (Colour online) Definition of an obliqueness angle based on the initial orientation.

where $\kappa = |\boldsymbol{\kappa}(0)| = \sqrt{\kappa_1^2 + \kappa_3^2}$ is the initial value of the wavenumber magnitude. Equation (2.42) in the non-dimensionalized temporal and spatial coordinates defined in (2.44) can be rewritten as

$$\frac{S^2}{\bar{a}^2\kappa^2}\frac{\partial^2\hat{p}}{\partial t^{*2}} = \frac{\partial^2\hat{p}}{\partial x_2^{*}} - \hat{p} + \left[\mathrm{i}\left(\frac{\kappa_1}{\kappa}\right)\frac{\partial S^*}{\partial x_2^*} + \left(\frac{\kappa_1}{\kappa}\right)^2 S^{*2}\right]\hat{p} + 2\mathrm{i}\left(\frac{\kappa_1}{\kappa}\right)\frac{\bar{\rho}}{\kappa}\hat{u}_2 S, \tag{2.45}$$

where $\bar{a} = \sqrt{\gamma\bar{p}/\bar{\rho}}$ is the speed of sound in the background flow and $S^* = \int_0^t S\,\mathrm{d}\xi$.

To identify the role of perturbation orientation in the evolution of compressible Poiseuille flow, we introduce two parameters. Firstly, referring to figure 1, the obliqueness angle β is defined as the angle between wave vector $\boldsymbol{\kappa}$ and the streamwise coordinate x_1, given by

$$\beta \equiv \cos^{-1}\left(\frac{\kappa_1}{\kappa}\right). \tag{2.46}$$

Secondly, the effect of compressibility on flow stability is characterized by gradient Mach number, M_g, defined by (Sarkar 1995):

$$M_g \equiv \frac{Sl}{\bar{a}} = \frac{S}{\bar{a}\kappa}. \tag{2.47}$$

Now (2.45) can be written in a form wherein the effects of Mach number and obliqueness can be easily identified:

$$M_g^2\frac{\partial^2\hat{p}}{\partial t^{*2}} = \frac{\partial^2\hat{p}}{\partial x_2^{*}} - \hat{p} + \left[\mathrm{i}\frac{\partial S^*}{\partial x_2^*}\cos\beta + S^{*2}\cos^2\beta\right]\hat{p} + 2\mathrm{i}\frac{\bar{\rho}}{\kappa}\hat{u}_2 S\cos\beta. \tag{2.48}$$

For the sake of convenience, the following normalizations for pressure and velocity amplitude are suggested by:

$$\hat{u}_i^* = \hat{u}_i/\bar{a}; \quad \hat{p}^* = \hat{p}/\bar{p}. \tag{2.49a,b}$$

These definitions and further mathematical manipulation of equations (2.39)–(2.42) lead to the following hyperbolic equation for pressure:

$$M_g^2 \frac{\partial^2 \hat{p}^*}{\partial t^{*2}} = \frac{\partial^2 \hat{p}^*}{\partial x_2^*} - \hat{p}^* + \left[\mathrm{i}\frac{\partial S^*}{\partial x_2^*}\cos\beta + S^{*2}\cos^2\beta\right]\hat{p}^* + 2\mathrm{i}\gamma\hat{u}_2^* M_g\cos\beta. \tag{2.50}$$

Similarly, the velocity perturbation evolution can be described by an inhomogeneous wave equation. Differentiating (2.40) twice with respect to time yields

$$M_g^2 \frac{\partial^2 \hat{u}_2^*}{\partial t^{*2}} = \frac{\partial^2 \hat{u}_2^*}{\partial x_2^{*2}} - \left[(\hat{u}_1^* - \hat{u}_2^* S^*)\cos^2\beta + \left(\hat{u}_3^*\sin\beta + \mathrm{i}\frac{\partial \hat{u}_2^*}{\partial x_2^*}\right)\cos\beta\right] S^* - \mathrm{i}\frac{\hat{p}^*}{\gamma} M_g\cos\beta, \tag{2.51}$$

where $S^* = S^*(X_2, t) = \int_0^t S(X_2)\,\mathrm{d}\xi$. Note that equations (2.50)–(2.51) describe the evolution of perturbation in any general planar compressible shear flow. These equations are not amenable to straightforward analytical solution. Instead, we seek valuable insight based on the form of the governing equations and by examination of the behaviour at certain asymptotic limits in a compressible Poiseuille flow.

First and foremost, based on the definition of the relevant Mach number M_g (2.47), three distinct regions in high-speed Poiseuille flow can be identified. In general, the shear in the near-wall regions is much higher than in the central region. In low-speed flows, the gradient Mach numbers throughout the channel will be less than unity and the flow field will be solenoidal in character. However, at higher speeds, the gradient Mach numbers in the near-wall region will exceed unity. These regions will exhibit strong pressure waves and dilatational velocity fluctuations. Clearly, the flow character in this region will be different from that in low-speed flows. In the central region of the channel, the gradients are low and hence M_g will be less than unity. The two near-wall dilatational regions are separated from the central region by $M_g \sim 1$ lines. It will be shown later that the perturbation velocity and vorticity features are indeed distinctly different in the low- and high-speed regions.

2.2.1. *Interaction between pressure and u_2' velocity*

To enable examination of the p'–u_2' interactions, we simplify the respective evolution equations to only the coupling terms:

$$\frac{\mathrm{d}\hat{u}_2}{\mathrm{d}t} \approx \mathrm{i}\kappa_1 \frac{\hat{p}}{\bar{\rho}} S^*, \tag{2.52}$$

$$\frac{\mathrm{d}\hat{p}}{\mathrm{d}t} \approx \mathrm{i}\kappa_1 \gamma \bar{p} \hat{u}_2 S^*. \tag{2.53}$$

It has been well-established in previous works (e.g. Livescu & Madnia 2004) that the u_2' velocity is predominantly dilatational. From these, the kinetic and potential energy equations can be derived:

$$\frac{\mathrm{d}}{\mathrm{d}t}\left[\bar{\rho}(\hat{u}_2\hat{u}_2^c)\right] = \mathrm{i}\kappa_1\left(\hat{u}_2^c\hat{p} - \hat{u}_2\hat{p}^c\right) S^*, \tag{2.54}$$

$$\frac{\mathrm{d}}{\mathrm{d}t}\left[\frac{\hat{p}\hat{p}^c}{\gamma\bar{p}}\right] = -\mathrm{i}\kappa_1\left(\hat{u}_2^c\hat{p} - \hat{u}_2\hat{p}^c\right)\int_0^t S\,\mathrm{d}\xi, \tag{2.55}$$

where $(\cdot)^c$ indicates the complex conjugate operation. Clearly, the p'–u_2' coupling is mediated by the streamwise wavenumber κ_1. The right-hand sides of equations (2.54) and (2.55) are identical in magnitude and opposite in sign. This indicates that p' and u_2' are coupled as a harmonic oscillator. Thus, the potential energy incumbent in the pressure perturbations and the dilatational kinetic energy in u_2' must be nearly equal over an oscillation cycle at the inviscid limit:

$$\operatorname{avg}({u_2'}^2) \approx \operatorname{avg}\left(\frac{p'}{\bar{\rho}\bar{a}}\right)^2. \tag{2.56}$$

This represents a state of equipartition which will be verified later by DNS results.

2.3. *Perturbation behaviour at different asymptotic limits*

2.3.1. *Spanwise modes ($\beta = 90$)*

First we examine spanwise perturbation modes: $\beta = \pi/2$; $\kappa_1 = 0$ and $\kappa_3 = 1$. For all such perturbations, equations (2.50) and (2.51) indicate a decoupling of the p' and u_2' fields at all Mach numbers as $\cos\beta = 0$. Referring to (2.39), it can be surmised that the u_1' component is also unaffected by pressure as $\kappa_1 = 0$. Clearly, both u_1' and u_2' fields are impervious to the pressure field. Thus, spanwise perturbation behaviour can be expected to be independent of Mach number. In the incompressible case, the pressure-free growth of spanwise modes is referred to as the lift-up mechanism by Ellingsen & Palm (1975), Landahl (1980) and Hanifi & Henningson (1998). Our analysis indicates that the lift-up mechanism is preserved intact at all incompressible and compressible Mach numbers.

2.3.2. *Streamwise modes ($\beta = 0$)*

Next we turn our attention to streamwise modes: $\beta = 0$; $\kappa_1 = 1$ and $\kappa_3 = 0$. It is well established in the literature that as $M_g \to 0$, equations (2.50)–(2.51) for streamwise perturbations ($\beta = 0$) lead to TS waves. At larger M_g, p' assumes a wave-like character as dictated by its evolution equation. The resulting u_2' field is not solenoidal, leading to dilatational velocity fluctuations. The pressure-induced oscillations in u_2' can be expected to have a profound effect on instability evolution as neither kinetic energy production or vorticity production can be sustained. One of the objectives of this work is to examine how the perturbation evolution is modified.

2.3.3. *Uniform shear flow*

To infer the behaviour of perturbation modes of intermediate degrees of obliqueness, further simplifications of the governing equations are needed. We examine the interactions in uniform shear flow as it is amenable to more rigorous mathematical treatment. In other words, we propose that a reasonable characterization of obliqueness effect on pressure–velocity interactions can be obtained by simplifying the shear as locally constant. This simplification is similar to the WKB-based local stability analysis of Lifschitz & Hameiri (1991). Baines, Majumdar & Mitsudera (1996) also invoke such a simplification in analysing the TS waves in incompressible flows. It must be reiterated that the objective here is to develop a qualitative understanding of the pressure–velocity interactions unencumbered by the complexities introduced by any spatial variation of shear. The utility and validity of the simplification can be assessed later by comparing the analytical outcome against DNS results that fully account for spatial variations of shear, viscous effects, etc.

A detailed analysis of these equations in homogeneous flows is performed by Kumar *et al.* (2014) and their conclusions on the effect of perturbation obliqueness on pressure–velocity interactions are now summarized. For an arbitrary oblique wave vector, we define the effective shear, the effective shear, S_e, as:

$$S_e = S \cos \beta. \tag{2.57}$$

Next, we define an effective gradient Mach number for a mode of arbitrary obliqueness:

$$M_g^e = \frac{S_e}{\bar{a}|\kappa|} = M_g \cos \beta. \tag{2.58}$$

The effective Mach number M_g^e of a perturbation mode, rather than the planar Mach number M_g, is the appropriate dimensionless parameter to characterize the pressure–velocity interactions.

At high effective Mach number ($M_g^e > 1$), there exist two distinct regimes of pressure–inertia interaction in the momentum equation. At early times $S_e t < \sqrt{M_g^e}$, pressure perturbation evolves too slowly to affect velocity perturbation evolution. This is called the pressure-released (PR) stage, Kumar *et al.* (2014). For a given planar Mach number and obliqueness angle, the duration of the pressure-released stage, t_{PR} is given by

$$0 < t_{PR} < \sqrt{M_g/\cos \beta}. \tag{2.59}$$

During this period, perturbations at all oblique angles can be expected to exhibit lift-up mechanism behaviour. This will be later verified using DNS results. Beyond this time, pressure evolves rapidly enough to counter the inertial effects. At this stage, p' and u_2' evolves as a simple harmonic oscillator.

2.4. *Summary of analysis*

We can now summarize the various inferences from the linear analysis.

(i) Irrespective of the gradient Mach number, spanwise ($\beta = 90°$ or $\kappa_1 = 0$) modes are unaffected by pressure. Thus, the lift-up mechanism is preserved intact at all Mach numbers.

(ii) For a given planar Mach number (M_0), streamwise ($\beta = 0°$ or $\kappa_3 = 0$) modes experience highest effective Mach number. Thus, streamwise modes that lead to TS waves in incompressible flows can be expected to experience most significant compressibility effects in high-speed flows.

(iii) Modes of increasing level of obliqueness can be expected to experience progressively decreasing compressibility effects. Indeed, there exists a critical obliqueness angle, β_c which experiences unit effective Mach number.

$$M_g^e(\beta_c) = 1; \quad \beta_c = \cos^{-1}\left(\frac{1}{M_0}\right). \tag{2.60}$$

β_c demarcates the perturbation–orientation space into two regions. All modes with $\beta < \beta_c$ are classified as supersonic as their effective Mach number is greater than unity. Modes with $\beta > \beta_c$ are identified as subsonic modes. Oblique modes with $\beta > \beta_c$ are likely to be less affected by compressibility and retain their subsonic character. Whereas, velocity perturbations of modes with $\beta < \beta_c$ are likely to be significantly affected by compressibility effects.

	U_0 (m s^{-1})	ρ_0 (kg m^{-3})	T (K)	Re	M
Case 1	705.2	0.02	61	65 700	4.5
Case 2	931.6	0.02	60	93 900	6.0
Case 3	1108.5	0.04	59	22 800	7.2

TABLE 1. Initial base flow conditions.

(iv) All perturbations experience an initial PR state. During this period, the behaviour is similar to that of lift-up modes. The duration of the PR state increases with Mach number and obliqueness angle. Compressibility effects manifest beyond this period.

(v) At high Mach numbers, p' and u'_2 are coupled as a harmonic oscillator and each variable will exhibit oscillatory behaviour. When averaged over long periods of time, the potential energy contained in p' and dilatation turbulent kinetic energy in u'_2 should be nearly equal – in a state of equipartition.

(vi) All of the above behaviour can be expected to manifest independent of the mode profile shape in the stream-normal direction.

We will next examine these analytical inferences by performing DNS of small perturbation evolution in parabolic Poiseuille flow. The DNS study incorporates both nonlinear and viscous effects not considered in the linear analysis.

3. Numerical scheme for DNS

Numerical simulations are performed using a gas kinetic method (GKM) solver. The GKM solves the Boltzmann equations for the single particle probability density function f using a linear collision operator (Xu 2001). The numerical discretization is applied to the fundamental quantity, the distribution function f, rather than the continuum variables. The constitutive relationships are computed as moments of the distribution function leading to consistent representations between various discretized conservation equations and precluding additional viscous/conductive flux discretization (May, Srinivasan & Jameson 2007). The main attribute of GKM is that it provides a good numerical platform for considering non-equilibrium and non-continuum effects. The current continuum-limit GKM code has been well tested in decaying and homogeneous turbulence flows (Kerimo & Girimaji 2007; Kumar, Girimaji & Kerimo 2013; Kumar *et al.* 2014). In these studies, the GKM compressible homogeneous shear turbulence DNS results are compared against RDT and previous simulations in the literature resulting in excellent agreement. In recent work (Xie & Girimaji 2014), the solver has been extended to wall-bounded shear flow. The background flow is sustained using a body force. A detailed verification and convergence study of the solver is presented in the Appendix.

Simulation parameters. In the current study, the computational domain is a rectangular box of dimension $L_{x_1} \times L_{x_2} \times L_{x_3} : 4L \times L \times 0.8L$. Grid cells are uniformly distributed along x_1 and x_3 directions. Along the wall-normal direction, x_2, the grids are distributed in geometric progression. The geometric progression coefficient is 1.0125. The grid is symmetric about the channel centreline. For all cases, the cell resolution is $N_{x_1} \times N_{x_2} \times N_{x_3} = 160 \times 200 \times 32$. The details of the simulation cases undertaken in the current study are given in table 1, where U_0 is the initial base flow velocity at the centreline, ρ_0 is the initial base flow density and T is the initial base flow temperature. The Mach number ($M_0 = U_0/\bar{a}$) is based on the centreline base velocity. The Reynolds ($Re = \rho U_0 L/\mu$) number is based on unit length scale. The various simulation parameters are chosen to be of the same order as that of Sivasubramanian & Fasel (2014). Further, these parameters fall into the range of flows that are investigated in the experimental facility at Texas A&M University (Tichenor, Humble & Bowersox 2013).

Boundary conditions. Periodic boundary conditions are applied in the x_1 and x_3 directions. In the x_2 direction, no-slip and no-penetration wall conditions are applied. Adiabatic and isothermal conditions are examined, and both boundary conditions yield similar perturbation evolution while the base temperature and density profiles show minor variations. Simulations performed using the isothermal wall condition are presented here similarly as the work of Xie & Girimaji (2014).

Initial conditions. A time-invariant parabolic base flow is first generated using a body force (Xie & Girimaji 2014). The body force is chosen such that pressure, density and temperature fields are initially spatially uniform (see table 1). A perturbation velocity field is superposed on the base flow and allowed to evolve. The body force is maintained to sustain the parabolic base flow. It is found that, even at the end of the simulation, the mean density and temperature fields are close to spatially uniform at all times under the given conditions. Thus, we isolate the effects of high Mach number effects from those due to variations in the background thermodynamic state.

The magnitude of initial perturbation is set to 0.5 % of the value of the centreline base velocity. The linear analysis of the previous section is valid for arbitrary perturbation profiles in the wall-normal x_2-direction. As mentioned before, the goal of the study is to examine the fundamental features of pressure–velocity interactions for any arbitrary initial perturbation. Towards that end, we focus on three different initial perturbation profiles.

(i) The incompressible Orr–Sommerfeld (OS) perturbation mode (Davey 1973) that leads to flow instability in low-speed flows. This is similar to the initial condition used by Liang, Premasuthan & Jameson (2009) to study the transition to turbulence in high-speed channel flow. In that study, it is demonstrated that the resulting high Mach number channel flow captures the essential features of near-wall behaviour. Further, the use of this initial condition permits direct comparison between well-established incompressible flow behaviour and its compressible counterpart. Such comparison serves to isolate the effect of compressibility without the complicating influence of other features.

(ii) Next we examine an arbitrary perturbation profile that satisfies the boundary conditions and divergence-free constraint initially:

$$u_1' \approx U_0 \sin\left(2\pi \frac{x_1}{L_{x_1}}\right) \sin\left(2\pi \frac{x_2}{L_{x_2}}\right), \tag{3.1}$$

$$u_2' \approx U_0 \left(\frac{L_{x_2}}{L_{x_1}}\right) \sin\left(2\pi \frac{x_1}{L_{x_1}}\right) \cos\left(2\pi \frac{x_2}{L_{x_2}} + 1\right), \tag{3.2}$$

$$u_3' = 0. \tag{3.3}$$

(iii) The third perturbation is taken to be a simple linear superposition of the arbitrary and OS profiles, called the combined mode.

If all three perturbation profiles yield similar pressure–velocity interactions which are also consistent with linear theory, then one can cautiously infer that to be the general behaviour.

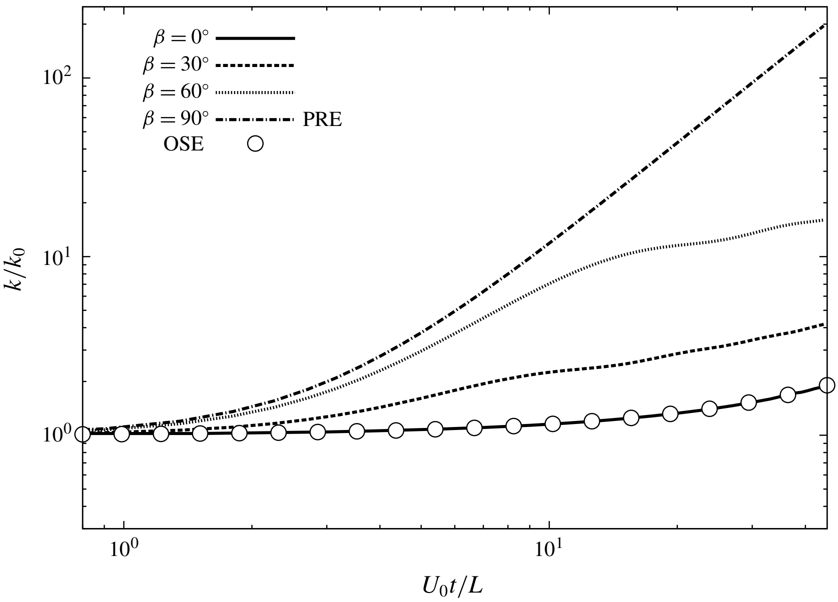

FIGURE 2. Kinetic energy evolution of oblique modes at $M_0 = 0.08$; OSE is the solution to the Orr–Sommerfeld equation for $\beta = 0°$.

4. Simulation results

The objective of the study is to contrast small perturbation evolution in low and high Mach number wall-bounded flows and explain the difference in the underlying flow mechanisms. Our interest here is confined to linear stability considerations. Thus only evolution of single initial perturbation mode is considered. Four investigations are undertaken:

(i) evolution of OS mode profile at low Mach numbers and different obliqueness angles;
(ii) evolution of OS mode profile at high Mach numbers and different obliqueness angles;
(iii) evolution of arbitrary mode profiles at high Mach number and different obliqueness angles;
(iv) effect of inhomogeneity on vorticity perturbation and the balance between linear and quadratic shear effects.

4.1. *OS mode evolutions at low Mach numbers*

Incompressible evolution of perturbations at different obliqueness angles with initial OS mode profile is first presented. This will serve as the baseline case for examining the compressibility effects. The volume-averaged turbulent kinetic energy evolution for various β values at the incompressible limit ($M_0 = 0.08$) is given in figure 2. The incompressible analytical OS solutions for $\beta = 0°$ is also plotted in figure 2. Through the rest of the paper, the behaviour $\beta = 0°$ mode is referred to as the solution to the Orr–Sommerfeld equation (OSE). Excellent agreement between linear theory and DNS is evident for the TS mode.

For $\beta = 90°$, the perturbation evolution exhibits more rapid growth. This is the lift-up behaviour discussed earlier in this paper (Landahl 1980). Perturbation modes with

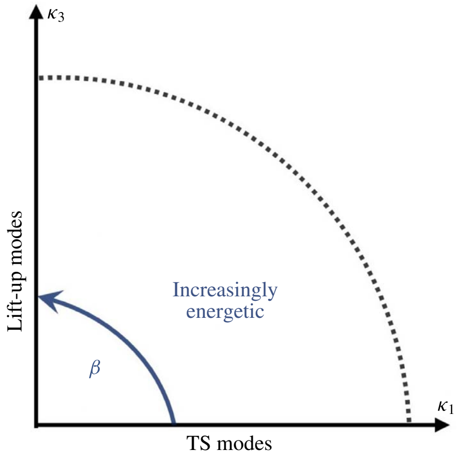

FIGURE 3. (Colour online) Dependence of growth rate on perturbation obliqueness in incompressible Poiseuille flow.

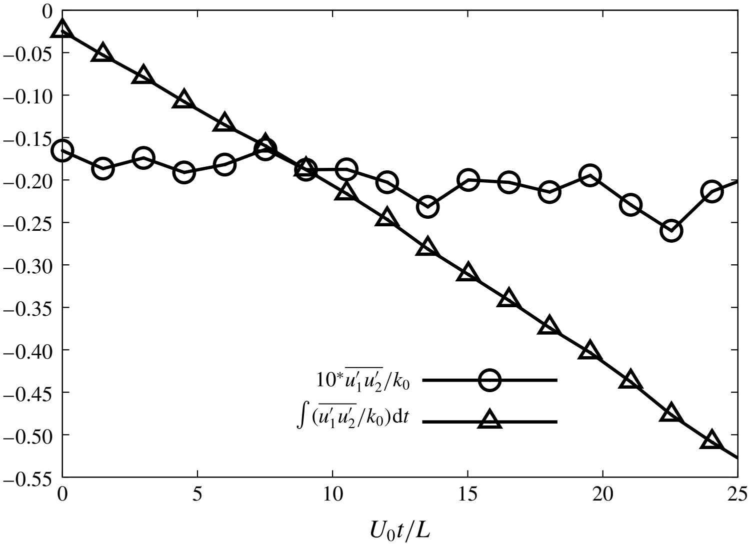

FIGURE 4. Shear Reynolds stress and its time integration evolution at $M_0 = 0.08$: Reynolds stress is scaled by 10.

intermediate angles also exhibit increasing growth rate at this low-speed limit. The growth rate of intermediate obliqueness modes fall between the limits set by TS and lift-up modes. Overall, perturbation modes of all obliqueness angles exhibit growth. The dependence of perturbation evolution on obliqueness angle in low-speed Poiseuille flow is summarized in the schematic in figure 3.

Reynolds shear stress $\overline{u_1'u_2'}$ plays an important role in the production of kinetic energy. Therefore, the evolution of shear Reynolds stress is examined for $\beta = 0°$ case at $x_2/L = 0.1$-plane. The Reynolds stress is obtained by plane averaging along the streamwise and spanwise directions. The Reynolds shear stress and its time-integral evolution are shown in figure 4. As previously stated, the normalized shear Reynolds

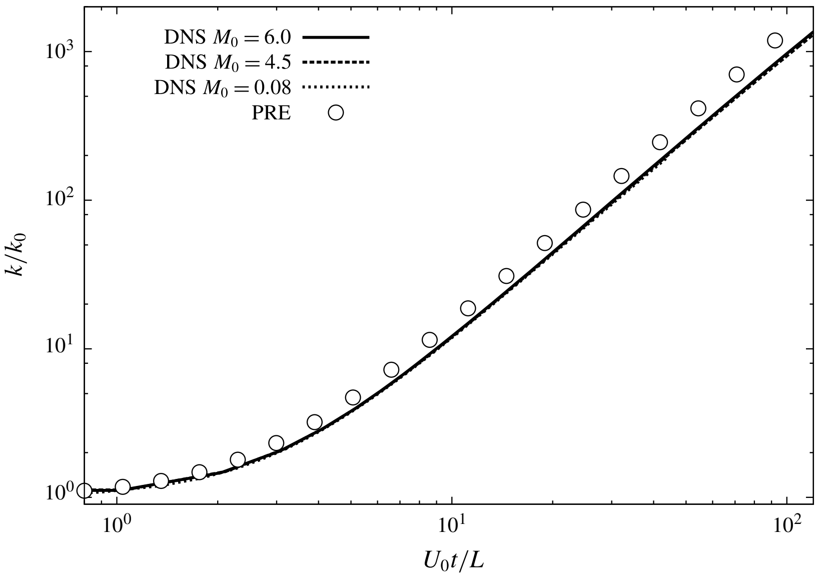

FIGURE 5. Kinetic energy evolution of spanwise perturbation.

stress is always negative and its time integral shows monotonic growth in magnitude with time. The time integral of $\overline{u_1'u_2'}$ corresponds to the total production of perturbation kinetic energy up to that point in time. This result will later be contrasted against the time integral of Reynolds shear stress in compressible flows.

4.2. *OS mode evolution at high Mach numbers*

Now we turn our attention to the evolution of OS profile modes in compressible flows. The OS perturbation is introduced at different obliqueness angles and the evolution is examined. The results are presented according to obliqueness angles.

4.2.1. *Lift-up mode* ($\beta = 90^\circ$)

Linear analysis clearly indicates that the evolution of spanwise modes should be nearly identical at all reference Mach numbers. The DNS results of volume-averaged turbulent kinetic energy evolution at $M_0 = 0.08$, 4.5 and 6 are shown in figure 5. The spanwise mode lift-up behaviour is indeed independent of Mach number. Furthermore, these results are in close agreement with the analytical solution of the pressure-released equation (PRE). The results clearly confirm that lift-up mechanism is intact at all Mach numbers.

4.2.2. *Streamwise mode* ($\beta = 0^\circ$)

We present the DNS results for volume-averaged turbulent kinetic energy as well as volume-averaged $u_1'^2$ in figure 6. The DNS results from computations at different Mach numbers are compared against OSE and PRE analytical solutions. Initially, the growth of all three Mach number cases are identical and follow the PRE solution, confirming the findings of the linear analysis. As explained earlier, the pressure perturbation effects are initially insignificant leading to a lift-up type of behaviour. The pressure fluctuations build up with time as the perturbations enter the second phase of their evolution. Then, the perturbation growth departs from the PRE limit as

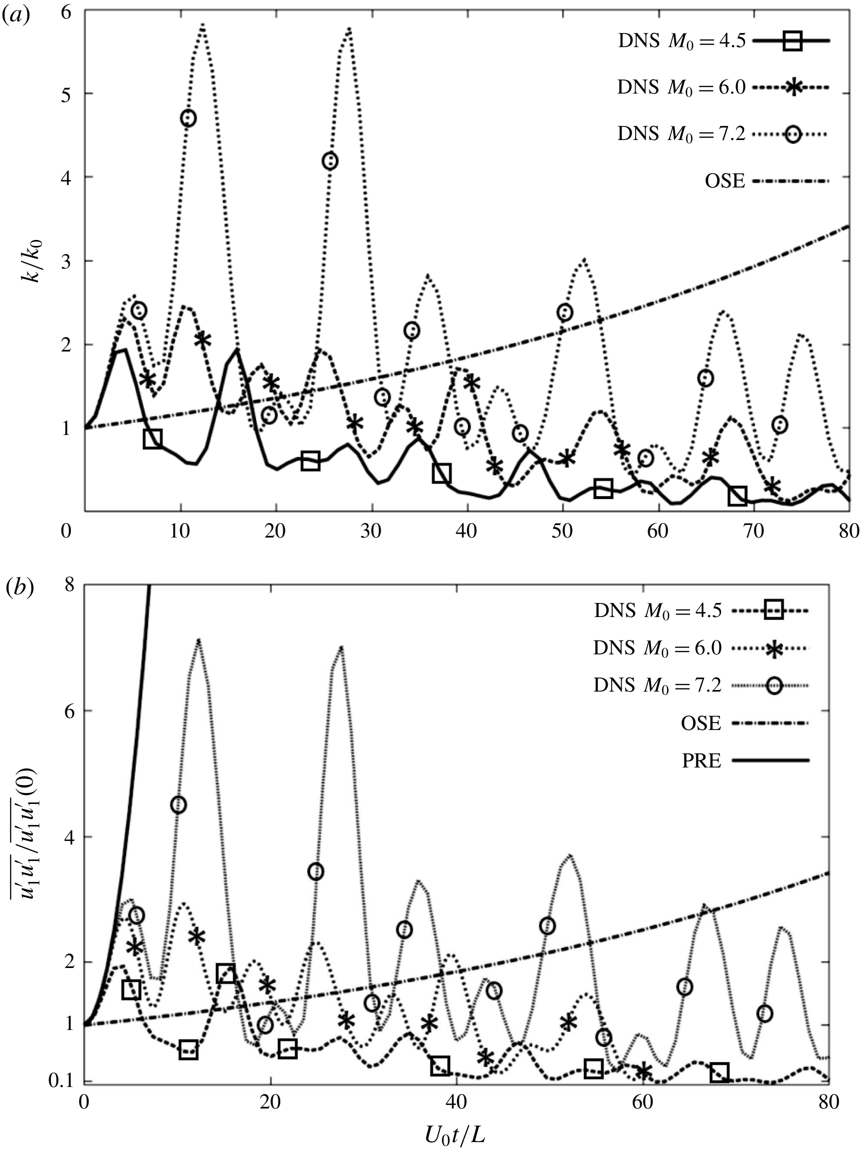

FIGURE 6. Evolution of streamwise perturbation in high Mach number flows: (*a*) turbulent kinetic energy and (*b*) $\overline{u_1'u_1'}$.

soon as the pressure effects become significant. The figure also shows that the higher the Mach number, the later is the departure from PRE behaviour, once again in line with the analysis presented in § 2. The subsequent evolution demonstrates oscillatory behaviour as suggested by the linear analysis due to the emergence of a dilatational velocity fluctuation. Eventually, the kinetic energy reduces to levels much lower than the TS perturbation energy in incompressible flow. It is evident that the instability is suppressed due to the action of the oscillatory dilatational field.

Now we seek the physical explanation underlying the stabilization of the streamwise perturbation mode. The linear analysis of § 2 indicates that the u_2' component is

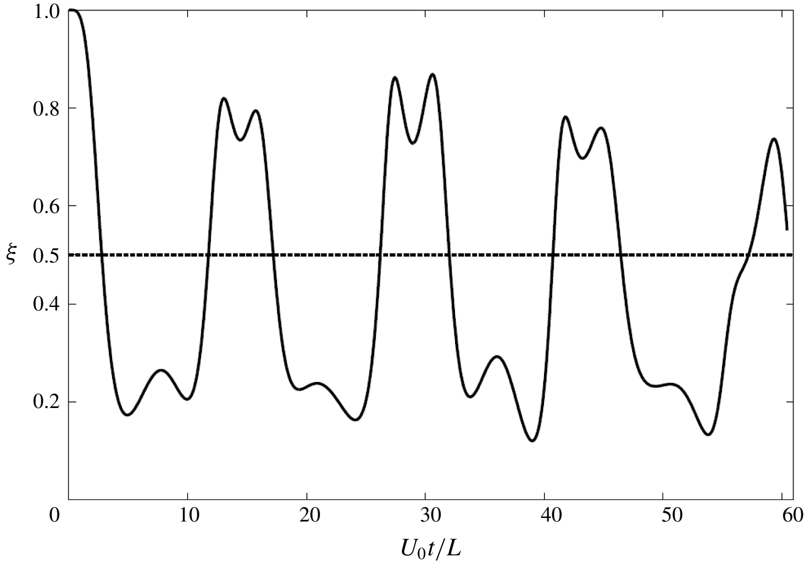

FIGURE 7. Energy equipartition between wall-normal velocity and pressure perturbation at $M_0 = 6$. $\xi = (\overline{u_2'u_2'})/(u_2'u_2' + \overline{p'p'}/(\gamma\rho\bar{p}))$.

coupled to pressure as in a harmonic oscillator leading to equipartition of energy between them. To verify this inference, in figure 7 we plot volume-averaged ${u_2'}^2$ and p'^2 for the case of $M_0 = 6$. As anticipated, the potential energy and dilatational kinetic energy oscillate about the equipartition level. Linear analysis further indicates that this behaviour should lead to oscillations in the all-important Reynolds shear stress $\overline{\rho u_1'u_2'}$.

The Reynolds stress component $\overline{\rho u_1'u_2'}$ is plotted in figure 8 as a function of time for $M_0 = 6$ case. The time integral of the stress is also shown as this corresponds to the total production up to that instant in time. The contrast between the incompressible (figure 4) and compressible (figure 8) shear stress evolution is immediately evident. Unlike its low Mach number counterpart, the compressible Reynolds stress shows large oscillations covering negative and positive values. As a result, the integral stays close to zero despite large initial excursions toward negative values. Thus, the kinetic energy does not exhibit sustained growth leading to stabilization. In summary, the streamwise perturbation mode is suppressed in high-speed flows due to the action of pressure which creates oscillations in $\overline{\rho u_1'u_2'}$ spanning both positive and negative values.

4.2.3. *Oblique modes* ($0° < \beta < 90°$)

For oblique modes with angles between 0° and 90°, the individual perturbations are investigated by examining the volume-averaged turbulent kinetic energy evolution shown in figure 9 for two Mach numbers. At early times modes, all oblique modes follow the PRE evolution for some duration. Consistent with linear analysis, the more oblique the mode, the longer is the duration of the PR (or lift-up) behaviour. At later times, the streamwise mode evolution exhibits the most oscillations due to the action of pressure. The oscillations become weaker with increasing β. Moreover, with increasing β, the perturbations become more energetic and approach the

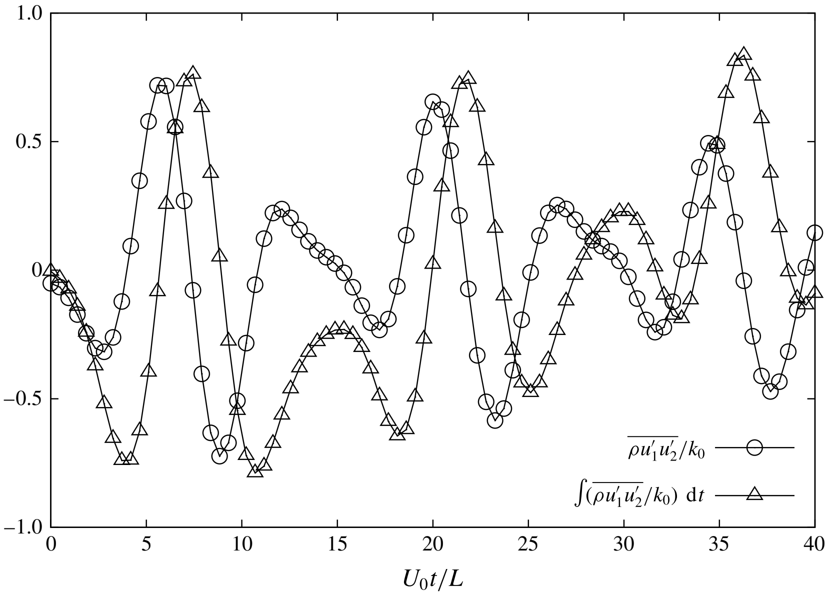

FIGURE 8. Shear Reynolds stress and its time integration evolution at $M_0 = 6$.

pressure-released limit at $\beta = 90^\circ$. This is completely consistent with linear theory wherein it is shown that the effective Mach number decreases with β, and the effect of compressibility diminishes correspondingly.

Next we investigate the significance of the critical angle (β_c) identified in the linear analyses. For $M_0 = 4.5$ and 6 cases, the β_c values are approximately 77° and 80° respectively. Referring to figure 9, the following observations can be made.

(i) For $\beta < \beta_c$, the computational results indicate asymptotic decline of kinetic energy. Evidently, this is due to the oscillatory coupling between u_2' and p'.

(ii) The kinetic energy of $\beta \geqslant \beta_c$ modes do not display oscillations. These modes are not discernibly suppressed by compressibility effects and their evolution is nearly similar to their incompressible counterparts. Most importantly, the growth continues over the duration of simulation. These findings are summarized in the schematic in figure 10.

All discussions thus far have focused on initial perturbation profile taken from the Orr–Sommerfeld analysis of an incompressible Poiseuille flow. The intent was to examine how TS waves (streamwise) and lift-up (spanwise) modes are affected at high speeds. Now we examine other perturbation profiles to ensure the validity of the inferences summarized above.

Kinetic energy evolution of arbitrary and combined perturbation modes, defined in § 3, is examined in figure 11 at $M_0 = 6$. It is evident that $\beta = 0^\circ$ perturbation is still suppressed. The large oscillations indicate the effect of dilatational velocity fluctuations. The $\beta = 90^\circ$ modes again grow monotonically and do not exhibit any Mach number effect. At intermediate angles, the growth rate gradually increase as indicated by linear analysis and summarized in the schematic in figure 10.

It is important to completely reconcile the PR stage with the lift-up mechanism in the literature. The connection can be surmised from the following observations.

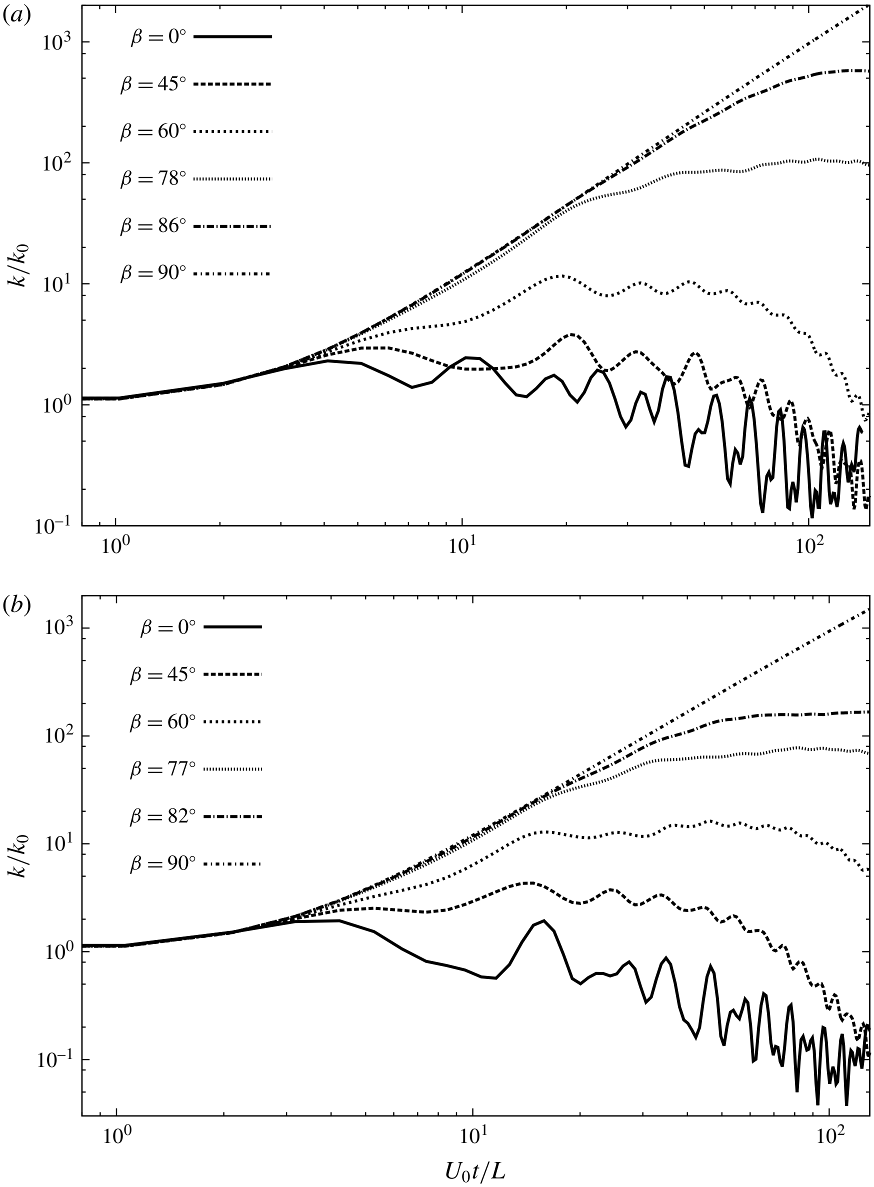

FIGURE 9. Kinetic energy evolution of oblique modes: (*a*) $M_0 = 6$ and (*b*) $M_0 = 4.5$.

(i) Spanwise perturbations of all supersonic Mach numbers experience a prolonged PR state and the kinetic energy exhibits algebraic growth (see figure 5). This is the well-established lift-up effect.

(ii) At high Mach numbers, modes of all angles experience a short duration of PR state. As established in the linear analysis, the duration of PR state increases with Mach number M_0 and obliqueness angle β. From figure 6, it is evident that even streamwise modes experience a lift-up type of growth at the early PR stage. Figures 9 and 11 demonstrate the effect of obliqueness and initial mode shape. From figure 9, it is evident that oblique modes exhibit lift-up behaviour for a

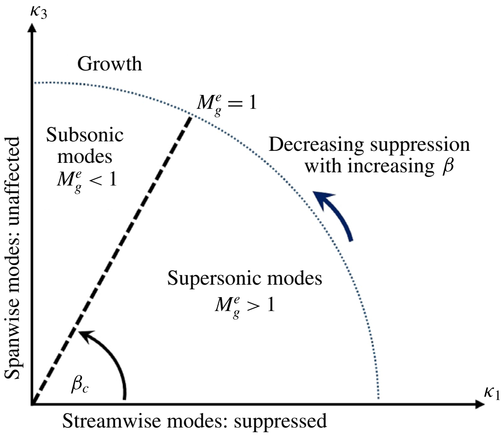

FIGURE 10. (Colour online) Dependence of kinetic energy growth rate on obliqueness in compressible Poiseuille flow.

longer duration as suggested by linear analysis. Figure 11 clearly demonstrates that the obliqueness effect is independent of the initial perturbation profile. Thus lift-up behaviour is seen at early times independent of Mach number (so long as it is high) and obliqueness.

(iii) The deviation from lift-up behaviour occurs due to the action of pressure. Pressure effects come into play faster at (i) lower Mach numbers; and (ii) lower obliqueness angles.

(iv) Equipartition (over a cycle of oscillation) is observed immediately following the PR stage.

4.3. *Effect of inhomogeneity on vorticity*

The results presented thus far are consistent with the linear analysis of the pressure equation in which the spatial variation of shear is neglected. To establish the effect of shear variation we examine the vorticity budget for $\beta = 0$ OS mode. This will provide further insight into how the incompressible perturbation vorticity is suppressed in compressible flows.

We focus on the spanwise vorticity equation given in (2.26). There are three important terms on the right-hand side of the equation as the viscous effect is not significant in the duration considered. As mentioned before, the baroclinic term and compressible vorticity production correspond to the compressibility effects. The second derivative term is pertinent in both the incompressible and compressible flow regimes. In high Mach number Poiseuille flow, the three mechanisms are examined using DNS data in figure 12. At a given time instant, a contour plot of each significant vorticity term in the x–y plane is shown. The planar root-mean-square of each term at that same instance is shown in figure 13. It is immediately evident that there are three distinct regions as suggested by linear analysis in § 2.2. Adjacent to each wall, there is a region in which CVP is completely dominant. It is in this region that TS waves typically develop in incompressible flows. Here, the compressible effects preclude the formation of such waves. In the central region, occupying 75 % of the channel height, the CVP and second derivative effects are nearly equal and out of phase. This region does not contribute much to the flow dynamics at any speed.

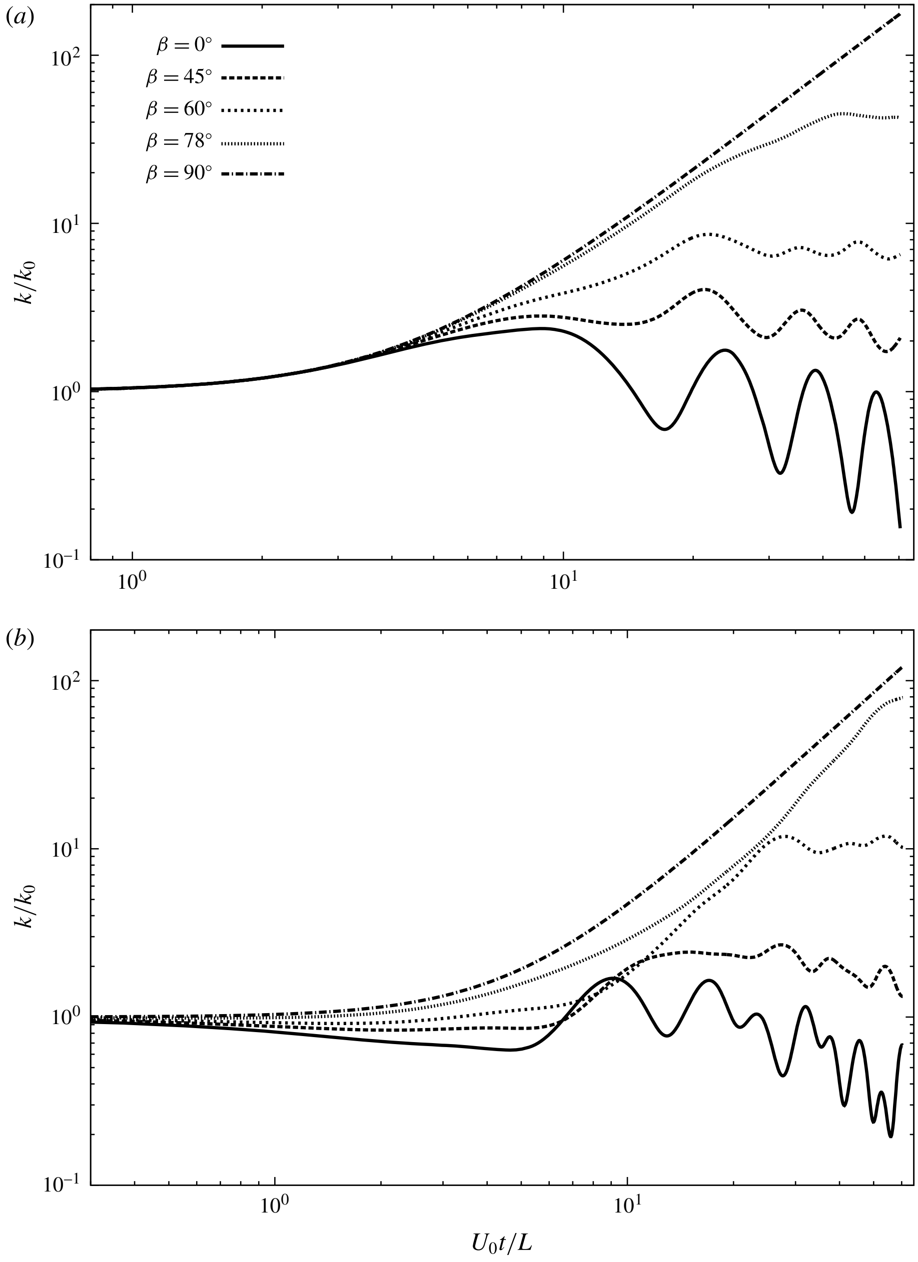

FIGURE 11. Evolution of kinetic energy for other initial modes at $M_0 = 6$: (*a*) arbitrary mode and (*b*) combined mode.

The baroclinic term is negligible at all locations. This is to be expected as background density variation is not considered in this study.

To examine the consequence of the CVP effect, the spanwise vorticity contours for both low- and high-speed Poiseuille flow are given in figure 14. The vorticity is normalized by the base flow centreline velocity U_0 and length scale L. In the incompressible case, a single vortex structure spans the entire channel height.

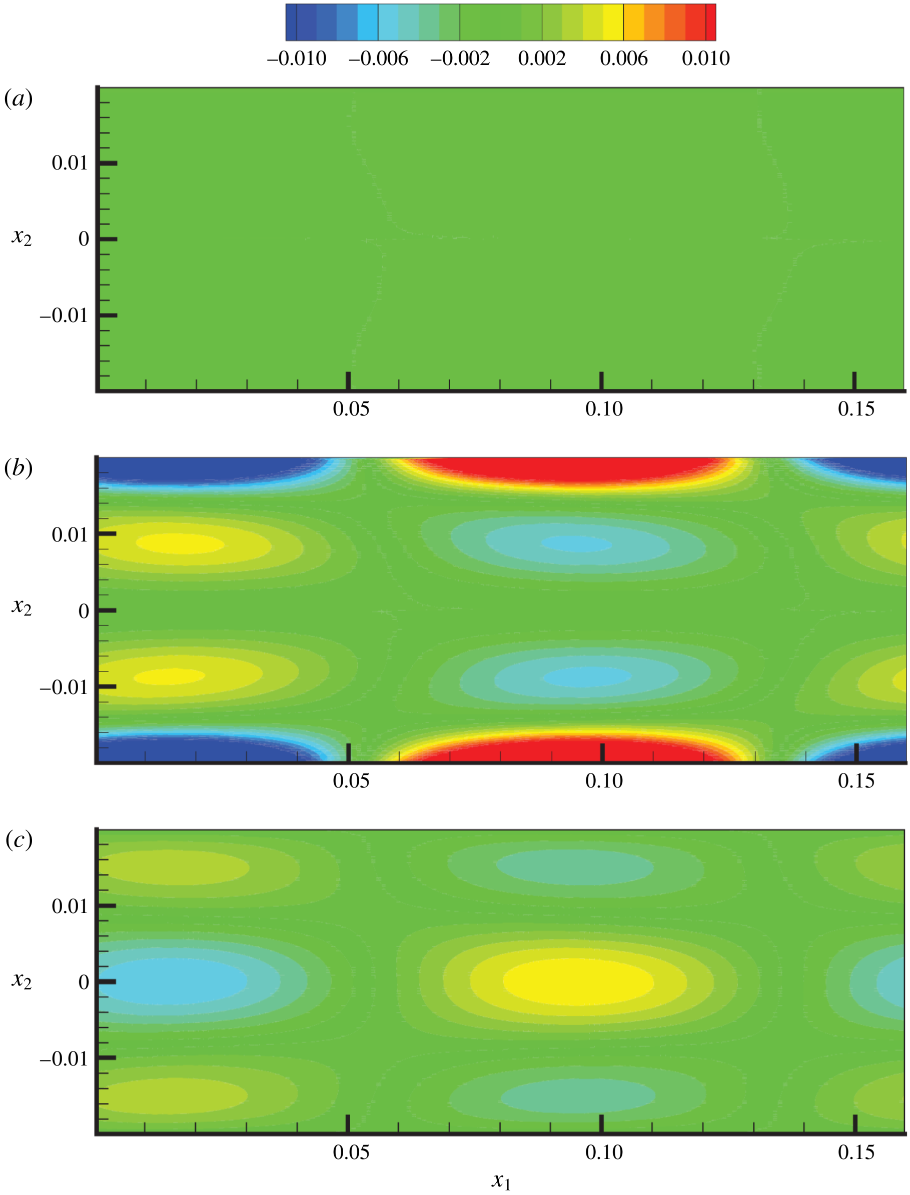

FIGURE 12. (Colour online) Spanwise vorticity budget term at $M_0 = 6$: (*a*) baroclinic term, (*b*) compressible vortex production term and (*c*) second derivative term.

On the other hand, the high Mach number case exhibits three distinct vortical structures across the channel height corresponding to the three regions of CVP identified in figure 12.

The corresponding perturbation velocity vectors are plotted in figure 15 for $M_0 = 0.08$ and 6. The difference in the structure at the two speeds is clearly evident. The circulation in the incompressible case covers the entire channel height resulting in efficient momentum transfer from the centre of the flow to the walls. The flow in the high-speed case is separated into three distinct regions across the channel height

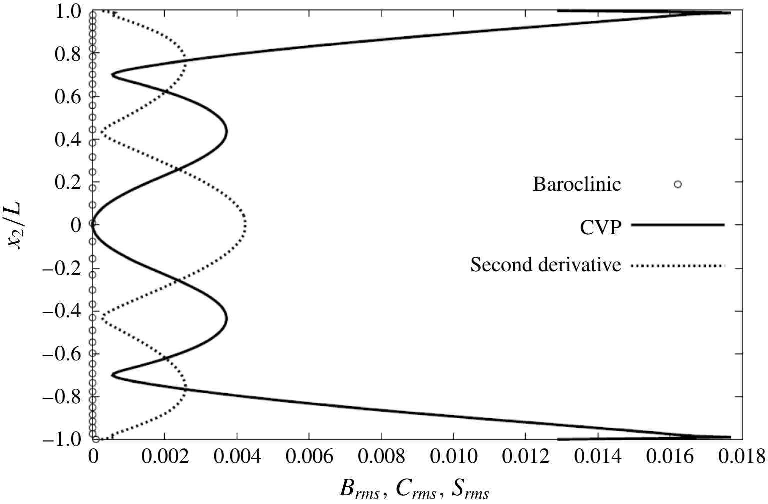

FIGURE 13. Root mean square of vorticity budget: baroclinic, CVP and the second derivative. All terms are defined in (2.26).

as previously observed. Each near-wall region exhibits pulsating motion within its domain. The circulation in the centre does not penetrate all the way to the wall. Therefore, there is reduced momentum mixing between the centre and the walls.

5. Conclusion

The objective of this work is to examine the effect of dilatational fluctuations on small perturbation growth in wall-bounded high-speed shear flows. The character of pressure–velocity interactions and the consequent effect on perturbation evolution is characterized at different flow speeds. Linear analysis of the pertinent initial value problem highlights the importance of perturbation obliqueness and leads to crucial inferences. The inferences are then examined using DNS of small perturbation evolution at different Mach numbers. The main conclusions are as follows.

(i) Spanwise perturbation mode evolution is impervious to Mach number in Poiseuille flows. Thus the lift-up mechanism is preserved intact in high-speed wall-bounded flows.

(ii) Streamwise disturbances that lead to TS waves at low speeds are profoundly affected by compressibility. The oscillatory nature of u_2' evolution prevents sustained growth of turbulent kinetic energy. These oscillations also prevent the formation of strong vortex structures in the near-wall region.

(iii) Perturbations of intermediate levels of obliqueness experience varying degrees of suppression. Indeed, perturbations aligned close to the spanwise direction experience subsonic Mach numbers and hence very limited suppression.

(iv) The potential energy incumbent in the pressure fluctuations and dilatational kinetic energy in the wall-normal velocity fluctuations are in a state of equipartition.

(v) The high-speed Poiseuille flow domain is partitioned into three different regions: two compressibility-dominated near-wall regions and a central region. The dilatational fluctuations in the near-wall regions isolate the wall from the central region leading to diminished momentum exchange.

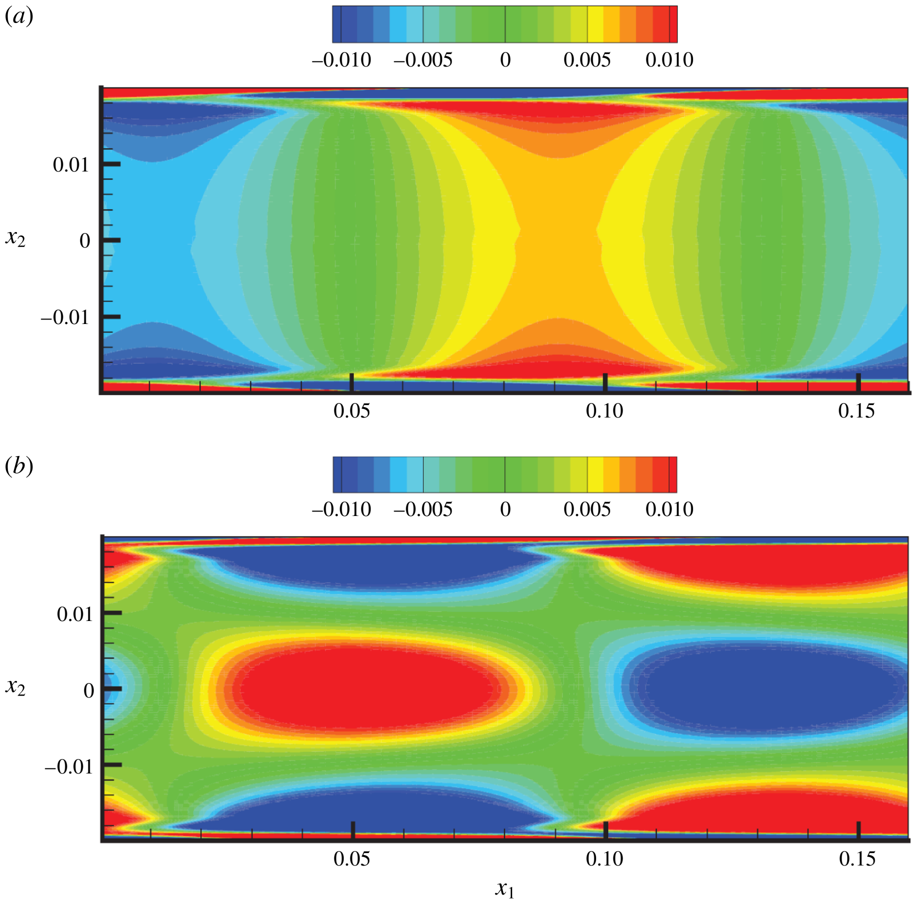

FIGURE 14. (Colour online) Spanwise vorticity contours in low-speed and high-speed flows: (*a*) $M_0 = 0.12$ and (*b*) $M_0 = 6$.

Development of closure models for predictive computations of transition and turbulence in high-speed flows requires an intimate knowledge of pressure action at different flow speeds. This work represents a first step in that direction. Pressure–strain correlation closure models based on these findings have already been developed and were found to be successful in the computation of high-speed boundary layers and mixing layers (Gomez & Girimaji 2013, 2014). While more work is needed to fully understand compressibility effects on transition to turbulence in high-speed wall-bounded flow, this work explicates some of the important pressure–velocity interactions and the consequent influence on perturbation evolution.

Acknowledgements

This work was supported by the National Center for Hypersonic Laminar-Turbulent Transition Research at Texas A&M University. The authors would like to thank Dr W. Saric for his support and guidance.

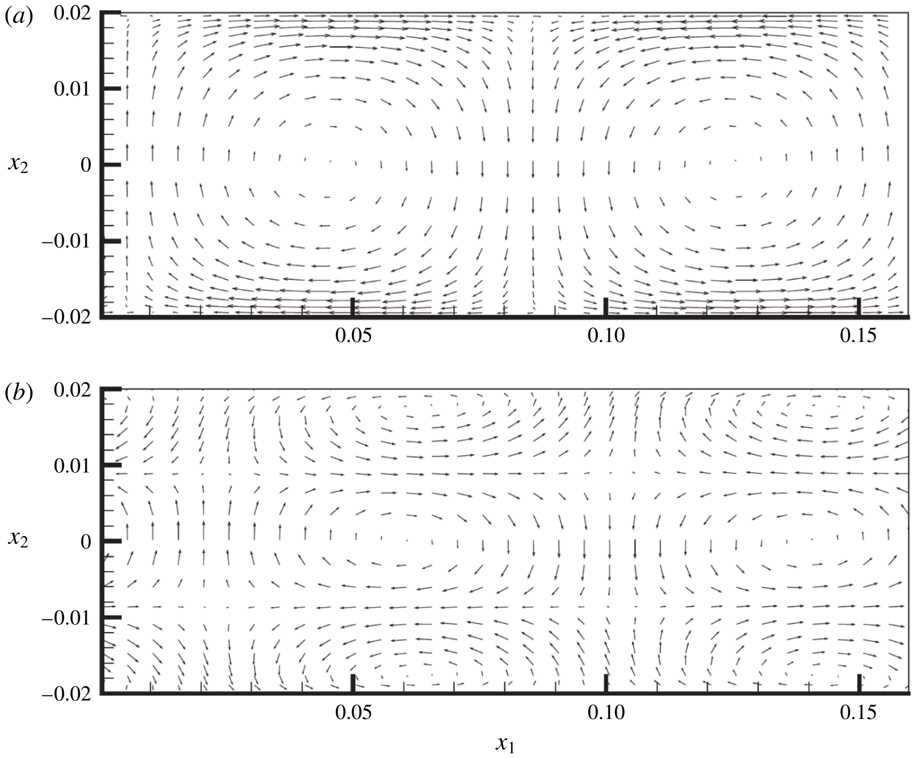

FIGURE 15. Typical flow structures of both low-speed and high-speed flow: (*a*) $M_0 = 0.12$ and (*b*) $M_0 = 6$.

Appendix. Numerical scheme validation and verification

At the low Mach number limit, the GKM results show excellent agreement with the OS solution in figure 5 of Xie & Girimaji (2014). Calculations with three initial perturbation levels are performed and the evolution of normalized perturbation magnitude from each case is compared against the analytical solution of the OSE. The numerical and analytical results are in excellent agreement, demonstrating the validity of the code at low speeds. Next we verify the code at the limit of very high Mach number. At the limit of high Mach number, the GKM results are compared against analytical solutions obtained from the PRE. For a detailed description of the pressure-released limit and PRE in wall-bounded flows, the reader is referred to Ellingsen & Palm (1975), Hanifi & Henningson (1998) and Xie & Girimaji (2014). It is shown that the GKM results for the three different Mach numbers agree well with the PRE analytical solution at the early stage when pressure effects are negligible (figure 2 of Xie & Girimaji (2014)). This is in complete agreement with the linear analysis results presented earlier in the paper. Moreover, the departure from the PRE solution scales according to theoretical estimate as shown by Xie & Girimaji (2014).

A convergence study for grid resolution and time step is performed and the results are shown in figure 16. Many different grid sizes and time steps are examined. The results are nearly grid independent at the resolutions and time steps used in the study.

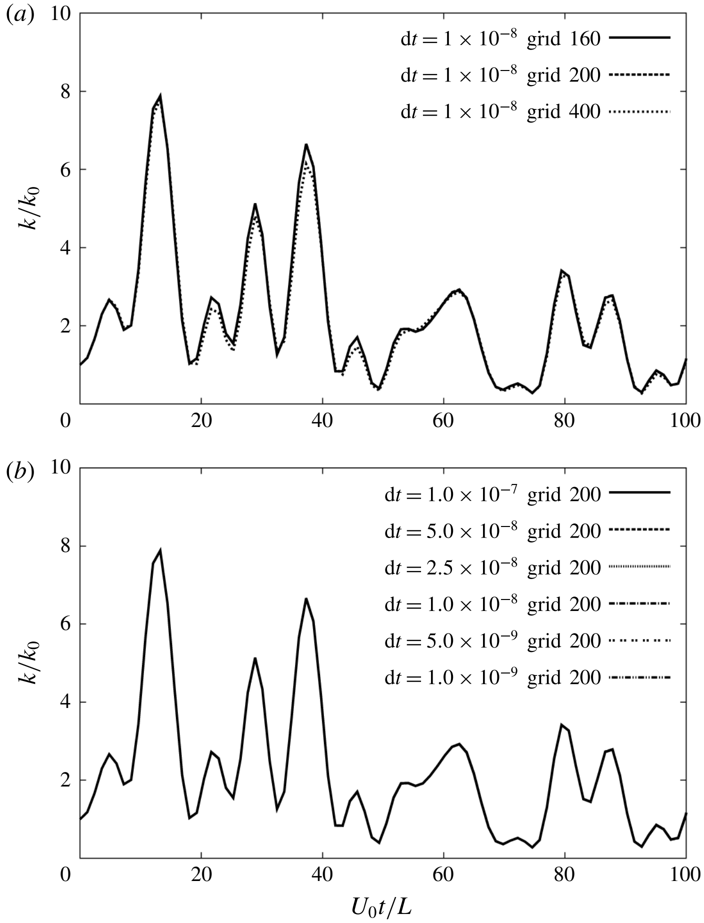

FIGURE 16. Convergence study at $M_0 = 8$: (*a*) grid resolution study and (*b*) time step study. k_0 is the initial perturbation kinetic energy. The number in the notation indicates the grid points in the wall-normal direction.

REFERENCES

BAINES, P. G., MAJUMDAR, S. J. & MITSUDERA, H. 1996 The mechanics of the Tollmien–Schlichting wave. *J. Fluid Mech.* **312**, 107–124.

BERTSCH, R. L., SUMAN, S. & GIRIMAJI, S. S. 2012 Rapid distortion analysis of high Mach number homogeneous shear flows: characterization of flow-thermodynamics interaction regimes. *Phys. Fluids* **24**, 125106.

BUTLER, K. M. & FARRELL, B. F. 1992 Three-dimensional optimal perturbations in viscous shear flow. *Phys. Fluids* A **4** (8), 1637–1650.

DAVEY, A. 1973 A simple numerical method for solving Orr–Sommerfeld problems. *Q. J. Mech. Appl. Maths* **26**, 401–411.

ELLINGSEN, T. & PALM, E. 1975 Stability of linear flow. *Phys. Fluids* **18** (4), 487–488.

GOMEZ, C. A. & GIRIMAJI, S. S. 2013 Toward second-moment closure modelling of compressible shear flows. *J. Fluid Mech.* **733**, 325–369.

GOMEZ, C. A. & GIRIMAJI, S. S. 2014 Explicit algebraic Reynolds stress model (earsm) for compressible shear flows. *Theor. Comput. Fluid Dyn.* **28** (2), 171–196.

HANIFI, A. & HENNINGSON, D. S. 1998 The compressible inviscid algebraic instability for streamwise independent disturbances. *Phys. Fluids* **10** (8), 1784–1786.

HEISER, W. H. & PRATT, D. T. 1994 *Hypersonic Airbreathing Propulsion*. AIAA.

HOWARTH, L. 1948 Concerning the effect of compressibility on laminar boundary layers and their separation. *Proc. R. Soc. Lond.* A **194** (1036), 16–42.

KARIMI, M. & GIRIMAJI, S. S. 2016 Suppression mechanism of Kelvin–Helmholtz instability in compressible fluid flows. *Phys. Rev.* E **93**, 041102.

KERIMO, J. & GIRIMAJI, S. S. 2007 Boltzmann-BGK approach to simulating weakly compressible 3D turbulence: comparison between lattice Boltzmann and gas kinetic methods. *J. Turbul.* **8** (46), 1–16.

KUMAR, G., BERTSCH, R. L. & GIRIMAJI, S. S. 2014 Stabilizing action of pressure in homogeneous compressible shear flows: effect of Mach number and perturbation obliqueness. *J. Fluid Mech.* **760**, 540–566.

KUMAR, G., BERTSCH, R., VENUGOPAL, V. & GIRIMAJI, S. S. 2015 Toward control of compressible shear flows: investigation of possible flow mechanisms. In *Advances in Computation, Modeling and Control of Transitional and Turbulent Flows*, pp. 397–404. World Scientific.

KUMAR, G., GIRIMAJI, S. S. & KERIMO, J. 2013 WENO-enhanced gas-kinetic scheme for direct simulations of compressible transition and turbulence. *J. Comput. Phys.* **234**, 499–523.

LANDAHL, M. T. 1980 A note on an algebraic instability of inviscid parallel shear flows. *J. Fluid Mech.* **98**, 243–251.

LAVIN, T. A., GIRIMAJI, S. S., SUMAN, S. & YU, H. 2012 Flow-thermodynamics interactions in rapidly-sheared compressible turbulence. *Theor. Comput. Fluid Dyn.* **26** (6), 501–522.

LEE, K., VENUGOPAL, V. & GIRIMAJI, S. S. 2016 Pressure-strain energy redistribution in compressible turbulence: return-to-isotropy versus kinetic-potential energy equipartition. *Phys. Scr.* **91**, 084006.

LIANG, C., PREMASUTHAN, S. & JAMESON, A. 2009 Large eddy simulation of compressible turbulent channel flow with spectral difference method. *AIAA Paper* 2009-402.

LIFSCHITZ, A. & HAMEIRI, E. 1991 Local stability conditions in fluid dynamics. *Phys. Fluids* A **3** (11), 2644–2651.

LIVESCU, D. & MADNIA, C. K. 2004 Small scale structure of homogeneous turbulent shear flow. *Phys. Fluids* **16** (8), 2864–2876.

MACK, L. M. 1984 Boundary-layer linear stability theory. *AGARD Report No.* 709.

MAY, G., SRINIVASAN, B. & JAMESON, A. 2007 An improved gas-kinetic BGK finite-volume method for three-dimensional transonic flow. *J. Comput. Phys.* **220**, 856–878.

REDDY, J. N. 1984 *Energy and Variational Methods in Applied Mechanics*. Wiley.

SARKAR, S. 1995 The stabilizing effect of compressibility in turbulent shear flow. *J. Fluid Mech.* **282**, 163–186.

SCHMID, P. J. & HENNINGSON, D. S. 2001 *Stability and Transition in Shear Flows*, Applied Mathematical Sciences, vol. 142. Springer.

SIMONE, A., COLEMAN, G. N. & CAMBON, C. 1997 The effect of compressibility on turbulent shear flow: a rapid-distortion-theory and direct-numerical-simulation study. *J. Fluid Mech.* **330**, 307–338.

SIVASUBRAMANIAN, J. & FASEL, H. F. 2014 Numerical investigation of the development of three-dimensional wavepackets in a sharp cone boundary layer at Mach 6. *J. Fluid Mech.* **756**, 600–649.

THOMSON, W. 1887 Stability of fluid motion: rectilinear motion of viscous fluid between two parallel planes. *Phil. Mag.* **24** (147), 188–196.

TICHENOR, N. R., HUMBLE, R. A. & BOWERSOX, R. D. W. 2013 Response of a hypersonic turbulent boundary layer to favourable pressure gradients. *J. Fluid Mech.* **722**, 187–213.

XIE, Z. & GIRIMAJI, S. S. 2014 Instability of Poiseuille flow at extreme Mach numbers: linear analysis and simulations. *Phys. Rev.* E. **89**, 043001.

XU, K. 2001 A gas-kinetic BGK scheme for the Navier–Stokes equations and its connection with artificial dissipation and Godunov method. *J. Comput. Phys.* **171** (1), 289–335.